Cobalt-site cerium doped $Sm_xSr_{1-x}CoO_{3-\delta}$ oxides as potential cathode materials for solid-oxide fuel cells

Guangru Zhang, Xueliang Dong, Zhengkun Liu, Wei Zhou, Zongping Shao, Wanqin Jin*

State Key Laboratory of Materials-Oriented Chemical Engineering, College of Chemistry and Chemical Engineering, Nanjing University of Technology, 5 Xinmofan Road, Nanjing 210009, PR China

ARTICLE INFO

ABSTRACT

A series of new oxides with the nominal composition of $Sm_xSr_{1-x}Co_{1-y}Ce_yO_{3-\delta}$ ($x = 0.1, 0.3, 0.5$; $y = 0.05$, 0.1) were synthesized. Their crystal structure, morphology, thermal expansion and electrochemical properties were systematically investigated. A phase-pure perovskite-type $Sm_{0.3}Sr_{0.7}Co_{0.95}Ce_{0.05}O_{3-\delta}$ oxide is obtained, while the other samples are actually composed of B-site cation deficient $Sm_xSr_{1-x}Co_{1-y}Ce_{y-z}O_{3-\delta}$ ($0 < z < y$) and CeO_2 mixed phases. These two-phase samples exhibit larger oxygen nonstoichiometry (δ) and higher average thermal expansion coefficients (TEC), while the single-phase $Sm_{0.3}Sr_{0.7}Co_{0.95}Ce_{0.05}O_{3-\delta}$ oxide shows a smaller δ and a lower TEC as compared to $Sm_{0.3}Sr_{0.7}CoO_{3-\delta}$. The introduction of cerium also effectively suppresses the chemical expansion and the growth of grain particles. The smaller grain size is beneficial in improving the electrode surface area. In addition, the electrical conductivities of Ce-doped $Sm_xSr_{1-x}CoO_{3-\delta}$ are all higher than $200\,S\,cm^{-1}$. EIS tests demonstrate that partially substituting Co with Ce and the B-site deficiency improve the cathode performance. $Sm_{0.3}Sr_{0.7}Co_{0.95}Ce_{0.05}O_{3-\delta}$ shows the lowest area specific resistance (ASR) among the others. Through proper cobalt-site cerium doping, the $Sm_xSr_{1-x}CoO_{3-\delta}$ related oxides could be developed into promising cathode materials for SOFC.

© 2009 Elsevier B.V. All rights reserved.

1. Introduction

Solid-oxide fuel cells (SOFCs) have several advantages over conventional power generation system, including higher energy efficiency and environmental friendliness [1]. Cathode is an important component of SOFCs and development of high-performance cathode is one of the key steps towards the wide spread of SOFC technology. In recent years, the application of perovskite-type oxides as cathode materials of intermediate-temperature (IT)-SOFCs has received increasing attentions [2–4] because of their high thermal stability as well as good thermal and chemical compatibility with solid electrolytes. Some perovskite oxides possess mixed oxygen ionic and electronic conductivity, which successfully extend the active oxygen reduction sites from the typical triple phase boundary (TPB) to the entire exposed cathode surface. As a result, an obvious reduction in electrode polarization resistance at low operation temperature is frequently observed. Among the many perovskites, $(LnSr)CoO_{3-\delta}$ (Ln: La, Pr, Sm, Gd) [3,5–7], $(LaSr)MnO_{3-\delta}$ [8], $(LaSr)(CoFe)O_{3-\delta}$ [9] and $(BaSr)(CoFe)O_{3-\delta}$ [10] have been the most widely investigated. It has been reported that Co-based perovskite oxide with relatively high ionic conductivity

exhibited higher electrochemical performance than the conventional Co-free materials such as $(LaSr)MnO_{3-\delta}$ at intermediate temperature. However, the average thermal expansion coefficients (TEC) of the Co-based perovskite-type materials are typically high, which limit their practical applications.

Strontium-doped samarium cobaltite with the compositions of $Sm_xSr_{1-x}CoO_{3-\delta}$ (SSC) show high electrical conductivity over a wide range of temperatures and have been extensively investigated as potential cathodes of IT-SOFCs recently. However, these materials have much larger TEC than the typical electrolytes such as samarium doped ceria (SDC) [6,11]. Several ways have been exploited to improve their compatibility with the electrolytes. Doping Fe or Mn into the B-site could lower the TEC. However, it also leads to a decrease in the electrical conductivity and an increase in the electrode polarization resistance [12]. The formation of a composite electrode by introducing an ionic conducting phase, typically with the same composition to that of electrolyte, is frequently adopted. Xia et al. [3] and Zhang et al. [13] demonstrated that the electrochemical performance of SSC was greatly improved when it formed composite with doped ceria. It is believed that introducing doped ceria to the SSC cathode could also decrease the TEC and improve the thermal compatibility with doped ceria electrolyte.

Herein, in order to make $Sm_xSr_{1-x}CoO_{3-\delta}$ cathodes more compatible with SDC electrolyte and improve the cathode performance, the cobalt-site doping with cerium was exploited. A new series

of oxides with the nominal composition of $Sm_xSr_{1-x}Co_{1-y}Ce_yO_{3-\delta}$ ($x = 0.1, 0.3, 0.5$; $y = 0.05, 0.1$) were synthesized. The effect of x and y on the crystal structure, morphology, thermal expansion, electrical conductivity, oxygen nonstoichiometry and electrochemical performance were systematically investigated.

2. Experimental

2.1. Sample preparation

Oxide powders with the nominal compositions of $Sm_xSr_{1-x}Co_{1-y}Ce_yO_{3-\delta}$ (SSCC) ($x = 0.1, 0.3$ and 0.5; $y = 0.05$ and 0.1) were prepared by a citric-EDTA complexing sol–gel method. The nitrates of Sm, Sr, Co and Ce were used (99.9% or higher) as the cation sources. EDTA was dissolved in $NH_3 \cdot H_2O$ at first and citric acid and stoichiometric nitrates were added afterwards. The molar ratio of EDTA, citric acid and metal ions was 1:1.5:1. $NH_3 \cdot H_2O$ was added to adjust the pH value to 6–7 and then a clear solution was obtained. After a drying process at 200 °C and with a combustion reaction, the water was removed and a spongy solid was formed. Finally, the obtained products were calcined at 950 °C for 5 h in air with the same heating and cooling rate of 2 °C min^{-1} to prepare the SSCC oxides. The powder samples were subjected to X-ray diffraction (XRD), iodometric titration and thermogravimetry (TG) characterization. The abbreviations of $Sm_xSr_{1-x}Co_{1-y}Ce_yO_{3-\delta}$ series are listed in Table 1.

The SSCC powders were grinded, sieved (300 meshes), and then uniaxially pressed at 400 MPa to prepare the green bars. After sintered at 1200 °C for 5 h in air with a heating and cooling rate of 2 °C min^{-1}, dense SSCC bars with the dimensions of ∼18 mm × 4 mm × 5 mm were obtained, which were adopted for the electrical conductivity and thermal expansion measurement.

The preparation procedures for the powder and green disk of $Sm_{0.2}Ce_{0.8}O_{1.9}$ (SDC) are similar to that of SSCC. After sintering the green disks at 1400 °C for 5 h in air, dense SDC electrolytes with a diameter of ∼13.0 mm and thickness of ∼0.5 mm were obtained. To fabricate the cathode layers, SSCC powder was dispersed in a mixture of ethylene glycol, ethanol and isopropyl alcohol with the help of high-energy ball mill (Fritsch Pulverisettle 6). The obtained suspension was deposited onto the both surfaces of SDC using the spray coating method. Symmetric SSCC-SDC-SSCC cells were obtained by calcined at 1000 °C for 2 h.
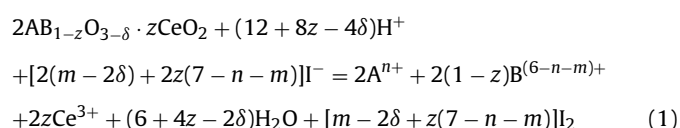
2.2. Characterization

The crystal phases of samples were determined by XRD with Cu Kα radiation (Bruker, model D8 Advance). The diffraction patterns were collected at room temperature in the range of $20° \leq \theta \leq 80°$ with the step width of 0.02° and scan rate of 0.5 s step^{-1}. The morphologies of porous cathodes were examined by scanning electron microscopy (SEM) (FEI, QUANTA-2000). The electrical conductivity of sintered specimens was measured in the stagnant air by a four-probe DC instrument (Keithley, model 2440 5A), where the Ag paste

and Ag wires were used to connect the sample and instrument. The thermal expansion behaviors of sintered specimens were measured using the apparatus of dilatometer (Netzsch, model DIL 402C). The heating rate was 5 °C min^{-1}. The weight changes of the samples were investigated up to 1100 °C with a heating rate of 10 °C min^{-1} in air atmosphere (50 ml min^{-1}) using a TG apparatus (NETZSCH STA 449 F3).

2.3. Iodometric titration

The room-temperature oxygen contents of SSCC were determined by iodometric titration method. In this method, approximate 50 mg of the sample were dissolved in 1 M HCl solution (∼100 ml) containing an excess of KI (∼2 g), resulting in the reduction of tri- and tetra-metal (Co^{4+}, Co^{3+}, Ce^{4+} to Co^{2+}, Ce^{3+}) and oxidation of I^- to I_2. The product I_2 was then titrated with sodium thiosulfate solution using starch as indicator. The whole process can be generally written as

$$2AB_{1-z}O_{3-\delta} \cdot zCeO_2 + (12 + 8z - 4\delta)H^+$$
$$+ [2(m - 2\delta) + 2z(7 - n - m)]I^- = 2A^{n+} + 2(1-z)B^{(6-n-m)+}$$
$$+ 2zCe^{3+} + (6 + 4z - 2\delta)H_2O + [m - 2\delta + z(7 - n - m)]I_2 \quad (1)$$

$$I_2 + 2S_2O_3^{2-} = 2I^- + S_4O_6^{2-} \quad (2)$$

where δ is the oxygen nonstoichiometry; z is the ratio of second phase in perovskite phase; n is the average oxidation state of A-site ions and m is the reduction amount of the oxidation state of B-site ions ($1 \leq n \leq 5$ and $1 \leq m \leq 6 - n$). For $(Sm_xSr_{1-x})(Co_{1-y}Ce_{y-z})O_{3-\delta} \cdot zCeO_2$, Sm^{3+}, Sr^{2+} and O^{2-} take fixed valence while Co and Ce were reduced to bivalent and trivalent, respectively. Therefore the oxygen nonstoichiometry can be written as:

$$\delta = \frac{CVM - [m + z(7 - n - m)]w_0}{16CV - 2w_0} \quad (3)$$

where w_0 is the mass of sample, M is the molar mass of $Sm_xSr_{1-x}Co_{1-y}Ce_{y-z}O_3 \cdot zCeO_2$, C is the molar concentration of $Na_2S_2O_3$ and V is the consumption of volume of the $Na_2S_2O_3$ solution.

2.4. Electrochemical impedance measurement

The polarization resistance and area specific resistance (ASR) of SSCC cathodes were characterized by the electrochemical impedance spectra (EIS) (Solartron 1287 potentiostat + Solartron 1260 frequency response analyzer). Silver paste (pre-diluted silver paste by alcohol) was painted to the electrode surfaces as current collectors. The applied frequency was in the range of 10 mHz to 10 kHz with a signal amplitude of 10 mV. Samples were tested under open circuit voltage condition in air atmosphere.

Table 1
Phase constituents, second phase CeO_2 content and evolution of peak $(1 1 0)_p$ in SSCC series.

Sample[a]	Symbol	Phases constituents	Ce ($y \times 10^2$ mol%)	CeO_2[b] ($z \times 10^2$ mol%)	2θ[c] $(1 1 0)_p$
$Sm_{0.5}Sr_{0.5}CoO_{3-\delta}$	SSCC55-10	Single-phase	0	0	33.36
$Sm_{0.5}Sr_{0.5}Co_{0.95}Ce_{0.05}O_{3-\delta}$	SSCC55-9505	Two-phase	5	1.25	33.08
$Sm_{0.5}Sr_{0.5}Co_{0.9}Ce_{0.1}O_{3-\delta}$	SSCC55-91	Two-phase	10	3.07	33.21
$Sm_{0.3}Sr_{0.7}CoO_{3-\delta}$	SSCC37-10	Single-phase	0	0	33.10
$Sm_{0.3}Sr_{0.7}Co_{0.95}Ce_{0.05}O_{3-\delta}$	SSCC37-9505	Single-phase	5	0	32.90
$Sm_{0.3}Sr_{0.7}Co_{0.9}Ce_{0.1}O_{3-\delta}$	SSCC37-91	Two-phase	10	2.42	32.83

[a] For convenient, using the nominal expression $Sm_xSr_{1-x}Co_{1-y}Ce_yO_{3-\delta}$ to represent the actual composition $Sm_xSr_{1-x}Co_{1-y}Ce_{y-z}O_{3-\delta} \cdot zCeO_2$ of two-phase samples.
[b] CeO_2 constituent in $Sm_xSr_{1-x}Co_{1-y}Ce_{y-z}O_{3-\delta} \cdot zCeO_2$ oxides.
[c] Diffraction angle 2θ of the characteristic peak $(1 1 0)_p$ of the perovskite phase.

3. Results and discussion

3.1. Crystal structure

Fig. 1 shows the XRD patterns of the oxides with the nominal composition of $Sm_xSr_{1-x}Co_{1-y}Ce_yO_{3-\delta}$. Samples with $y = 0$ show
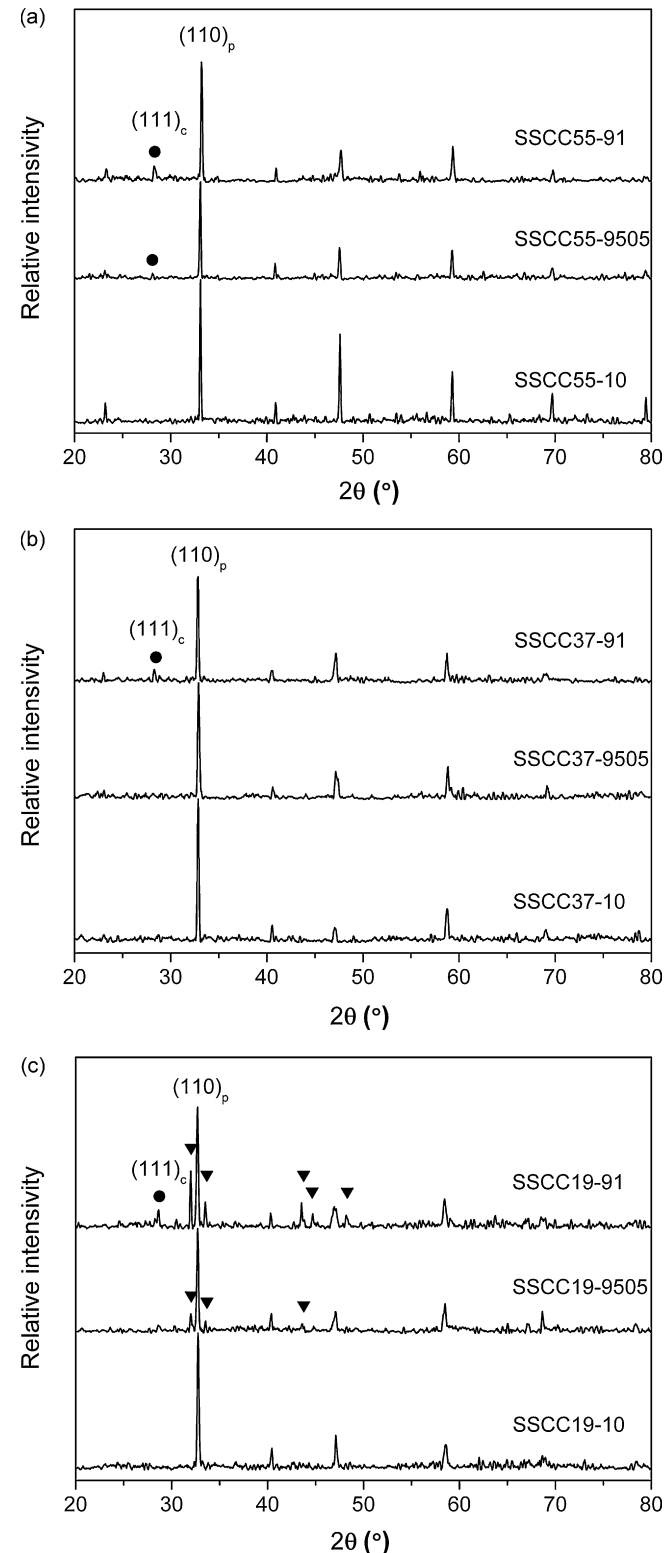

Fig. 1. XRD patterns of SSCC powders calcined at 950 °C for 5 h in air: (a) $x = 0.5$; (b) $x = 0.3$; (c) $x = 0.1$. (●) CeO_2; (▼) Sr–Ce–Co–O, $(1\,1\,0)_p$ is the peak in perovskite phase and $(1\,1\,1)_c$ is the peak in CeO_2 phase.

single-phase cubic perovskite structure. As shown in Fig. 1a and b, a phase-pure perovskite-type SSCC37-9505 oxide was obtained, while the other samples of SSCC55-9505 and SSCC55-91 contained a trace amount of CeO_2 phase. At a certain doping amount of Ce, the diffraction intensities of CeO_2 become weaker as the amount of Sm decreased. In Fig. 1c, an impurity was detected at $2\theta \approx 32°$ and 33.5°, which, to our knowledge, did not match any known phase(s) according to the powder XRD data. However, based on the fact that the diffraction peak intensity of the impurity decreased with the decrease of Sr or Ce content, it's reasonable to believe that the impurity phase is a compound or a mixture consists of the elements Sr, Ce, Co and O. This Sr–Ce–Co–O phase may be attributed to a serious solid state reaction between Ce and Sr related oxides.

The introduced cerium in the nominal composition $Sm_xSr_{1-x}Co_{1-y}Ce_yO_{3-\delta}$ is not totally incorporated in the perovskite lattice. The excess cerium is formed in CeO_2 in small quantities. Therefore, samples with $x = 0.3$ and 0.5 can be expressed in terms of a two-phase mixture with the composition of $Sm_xSr_{1-x}Co_{1-y}Ce_{y-z}O_{3-\delta} \cdot zCeO_2$ ($0 < z < y$), where z is the ratio of CeO_2 phase in SSCC perovskite phase. The CeO_2 content in each sample is approximately calculated by a direct comparison method [14]. The relationship between the phases α and β in the mixture is

$$\frac{I_\alpha}{I_\beta} = \frac{R_\alpha c_\alpha}{R_\beta c_\beta} \tag{4}$$

where I is the integrated intensity of the diffraction peak, c is the volume fraction of specific phase, and R depends on the nature of the phase, Bragg angle θ and miller indices $h\,k\,l$. Further, since $c_\alpha + c_\beta = 1$, the value of c_α (or c_β) can be obtained. Herein, the strongest peaks of $(1\,1\,0)_p$ peak in perovskite phase and $(1\,1\,1)_c$ peak in CeO_2 phase are considered to estimate the amount of the CeO_2 phase in the mixture. The results are listed in Table 1.

The appearance of CeO_2 phase indicated a high solution energy for Ce doping into the B-site, which is due to a large difference between the Ce ion ($r_{Ce^{4+}} = 0.87$ Å) and Co ion ($r_{Co^{4+}} = 0.53$ Å) [15]. Attfield et al. [16] reviewed the A cation size effects in the perovskite oxides and concluded that with the increase of the A cation size, the strain between the B cations decreased and therefore easily for B-site doping. The Sr ion ($r_{Sr^{2+}} = 1.12$ Å) is larger than the Sm ion ($r_{Sm^{3+}} = 0.958$ Å) and the average A cation size $\langle r_A \rangle$ increased as the content of Sr increased. Therefore, when x is lower (namely the Sr content is higher), Ce ions would be more easily doped into the B-site.

The evolution of the characteristic peaks $(1\,1\,0)_p$ in the perovskite phase with the variation of x and y is shown in Table 1. It's obvious that peaks $(1\,1\,0)_p$ of Ce-doped SSC with $x = 0.5$ and 0.3, respectively, appear to shift towards lower diffraction angles compared with that of undoped SSC, indicating that the lattice parameters increased as Ce doped into the B-site. Considering the significant difference in ionic radius between Co ($r_{Co^{4+}} = 0.53$ Å) and Ce ($r_{Ce^{4+}} = 0.87$ Å), partially substituted Co with Ce would cause an increase of lattice parameter and consequently a peak shift towards the lower diffraction angle. Therefore, for samples with $x = 0.3$, the peak angles decreased with the Ce content increased. The variation of lattice parameter may result from not only the difference of ionic radius but also the concentration of B-site deficiency. A high B-site deficiency concentration would cause the shrinkage of lattice [17]. At certain doping amount of Ce, the B-site deficiency concentration of samples with $x = 0.5$ are higher than that of samples with $x = 0.3$. Therefore, the higher B-site deficiency concentration would be a significant factor of the variation of lattice parameter for samples with $x = 0.5$. From Table 1, the peak angle of SSCC55-91 is actually between that of SSCC55-10 and SSCC55-9505, which may be due to the highest B-site deficiency concentration of SSCC55-91.

Table 2
The oxygen nonstoichiometry of SSCC obtained by iodometric titration at room temperature.

Sample	δ
SSCC55-10	0.11
SSCC55-9505	0.14
SSCC55-91	0.28
SSCC37-10	0.30
SSCC37-9505	0.27
SSCC37-91	0.36

3.2. Oxygen nonstoichiometry

Table 2 gives the oxygen nonstoichiometry δ of SSCC obtained by iodometric titration at room temperature. As Ce content increased, the nonstoichiometry δ of samples with $x = 0.5$ increased, while that of samples with $x = 0.3$ decreased firstly and then increased. SSCC37-9505 with a phase-pure perovskite-type structure has the lowest δ as compared with other two samples SSCC37-10 and SSCC37-91. Due to the charge compensation, the B-site cation deficiency would introduce additional oxygen vacancies [17] (often described in terms of oxygen nonstoichiometry δ). Therefore, the nonstoichiometry δ and oxygen vacancies of two-phase samples increased as the z in $Sm_xSr_{1-x}Co_{1-y}Ce_{y-z}O_{3-\delta} \cdot zCeO_2$ increased, namely as the amount of Ce increased.

Fig. 2 is the thermal gravimetric curves and oxygen nonstoichiometry of SSCC oxides obtained up to $1100\,^{\circ}C$ in air. Because the weight of CeO_2 was constant in air [18], the weight loss mainly stemmed from the $Sm_xSr_{1-x}Co_{1-y}Ce_{y-z}O_{3-\delta}$ perovskite phase. As can be seen from Fig. 2a and b, the weight of SSCC decreased with the increase of temperature. The nonstoichiometry δ of each sam-

ple at high temperature can be calculated by combining the oxygen contents at room temperature and weight loss in heating process. At any temperature in the heating process, the variation tendency of the nonstoichiometry δ is similar to that collected by iodometric titration at room temperature. The thermal expansion behavior, electrical conductivity and cathode performance have a strong correlation with the oxygen nonstoichiometry and oxygen vacancy concentration, which will be detailed later.

3.3. Thermal expansion behavior

Fig. 3 illustrates the total thermal expansion behaviors and instantaneous thermal expansion coefficient curves of SSCC. The data were obtained upon heating from 200 to $1000\,^{\circ}C$ in air. All the expansion curves show gradual increase as the temperature increased. As can be seen from Fig. 4, compared with the undoped SSC, the TEC ($200–1000\,^{\circ}C$) of two-phase samples with $x = 0.3$ or 0.5 increased slightly as the Ce content increased. Especially for sample SSCC37-9505, decreases in thermal expansion and TEC were observed. As shown in Fig. 3, the thermal expansion curves deviated from linearity between 450 and $650\,^{\circ}C$, which presented as a sudden increase of their slopes. This nonlinear change behaved as a drastic jump in the instantaneous thermal expansion coefficient curves. Thermal expansion in the oxygen deficient perovskites can be attributed to two mechanisms. We denote the onset temperature of the nonlinear change as T_0. When the temperature below T_0, the thermal expansion is mainly due to the atomic vibrations of lattice in heating process. The drastic increasing in thermal expansion above T_0 is mainly attributed to the chemical expansion, which
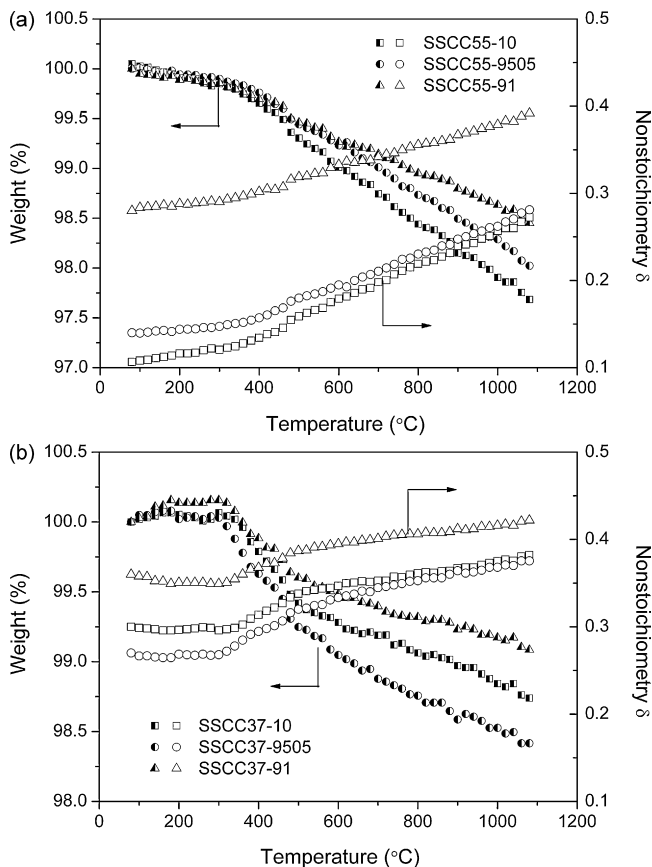

Fig. 2. Temperature dependence of TG curves and oxygen nonstoichiometry of SSCC oxides up to $1100\,^{\circ}C$ in air: (a) $x = 0.5$; (b) $x = 0.3$.
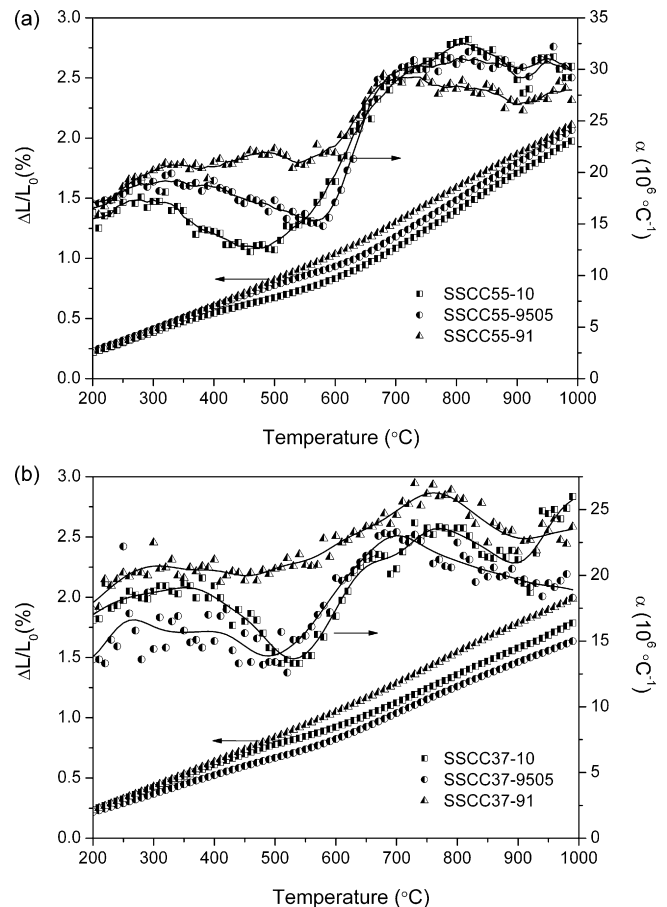

Fig. 3. Total thermal expansion behaviors and instantaneous thermal expansion coefficient curves of SSCC in air: (a) $x = 0.5$; (b) $x = 0.3$.
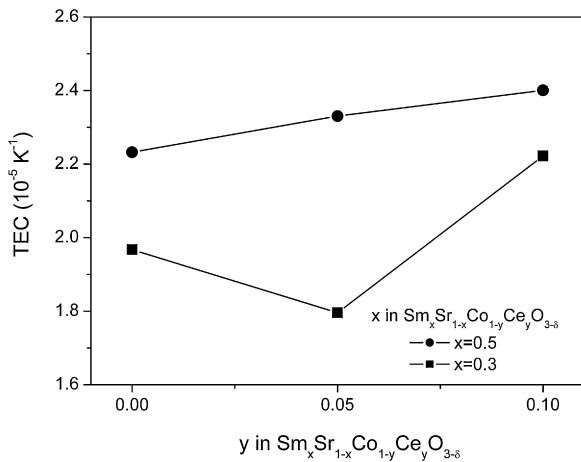
Fig. 4. Average thermal expansion coefficients of SSCC in the temperature range of 200–1000 °C.

Fig. 6. Arrhenius plots of electrical conductivity of SSCC.

was caused by the great amount lattice oxygen loss at the vicinity of T_0 [19–21]. Obviously, in Fig. 3, the nonlinear change is lightened and the jump height is decreased with Ce content increased. Therefore, the introduction of Ce could effectively suppressed chemical expansion.

The oxygen loss, accompanied by the generation of oxygen vacancies, exhibits an increase of nonstoichiometry δ. In order to maintain the electrical neutrality, a reduction of Co cation (Co^{4+} to Co^{3+}) would occur. Because the ionic radii of lower valence states Co^{3+} are larger than that of higher valence state counterparts, the thermal expansion behavior is enhanced. Therefore, the variation of TEC is strongly associated with the oxygen loss and thereby the variation of nonstoichiometry δ. For two-phase samples, the increase of Ce content and thereby the increase of δ would lead to an increase of thermal expansion. While for single-phase SSCC37-9505, with a lower nonstoichiometry than that of SSCC37-10, the thermal expansion declined.

3.4. Electrical conductivity

Fig. 5 is the temperature dependence of the total electrical conductivity for SSCC. The conductivities of undoped SSC are consistent with the literature reports [6,11]. SSCC55-10 showed the highest electrical conductivity among the others at whole temperature range under investigation. For samples with $x = 0.3$ or $x = 0.5$, the electrical conductivities decreased as the Ce content increased. In
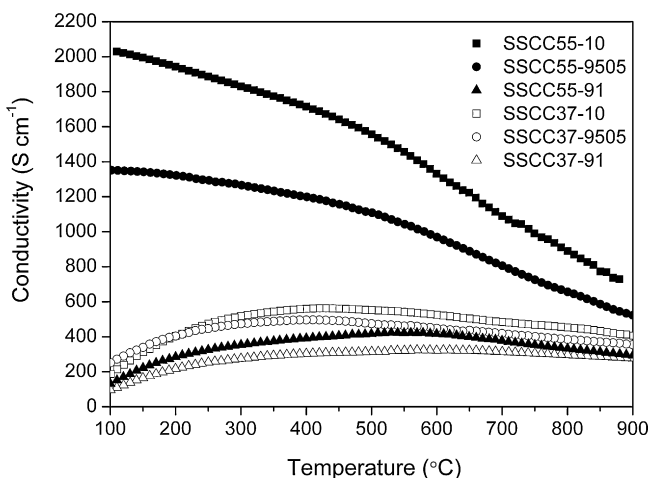

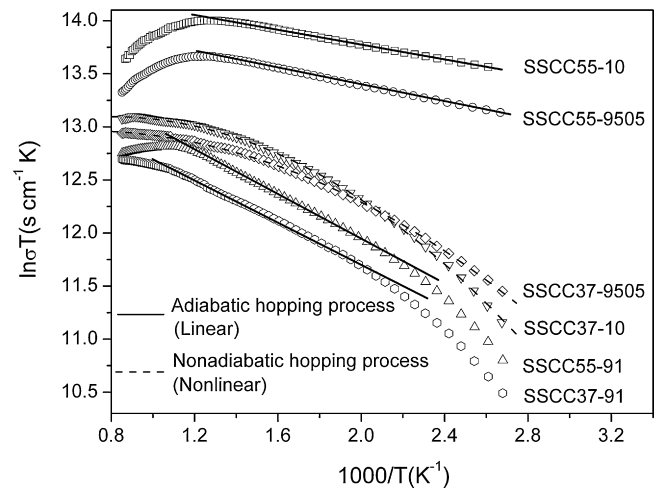**Fig. 5.** Temperature dependence of the electrical conductivity of SSCC in air.

addition, the electrical conductivities of Ce-doped SSC are all higher than $200 \, S \, cm^{-1}$.

The conductivity observed in perovskite-type oxide is based on the mechanism of Zerner double exchange [22]. The electrons/holes (charge carriers) transport indirectly between B ions via O ion namely along the –B–O–B–. The formation of oxygen vacancies accompanied by the decrease of the charge carrier concentration and absence of oxygen ions "O", and the B-site deficiency of two-phase samples would break the chain of –B–O–B– for electron/hole transport. These factors result in the drop of electrical conductivity. In this study, for two-phase samples with $x = 0.3$ or 0.5, the nonstoichiometry δ and oxygen vacancies increased with the increase of Ce content and consequently resulted in the drops of electrical conductivities. Furthermore, the poor conducting second phase CeO_2 might block the electron transport and contribute to decrease the electrical conductivity.

However, SSCC37-9505 which has a smaller oxygen nonstoichiometry δ than SSCC37-10 has a decrease of electrical conductivity. This can be understood by the barriers for carrier transport chain –Co–O–Co– where the Co-site was partially occupied by Ce ions. Perovskite-type oxides, where the bonding reaction occurred between A/B and O elements, have a mixture of covalent and ionic bonding. As the electronegative difference ΔE between A/B and O increased, the bonding become more ionic and more polar. The fraction of covalent bonding can be estimated from the equation [23]:

$$Fraction \; covalent = \exp(-0.25 \cdot \Delta E^2) \qquad (5)$$

Due to the difference between electronegative of B-site element (Ce $\sim$ 1.1, Co $\sim$ 1.9) and O ($\sim$3.5) (see Ref. [23]), the fraction covalent of Ce–O is approximate 55% smaller than Co–O. The stronger polarization of B–O may trap the transport of carriers and consequently decrease the electrical conductivity. Similar findings were reported by Vashook et al. in Ni doped (LaCa)MnO$_{3-\delta}$ system [24].

In general, the mechanism of temperature dependence of electrical conductivity of perovskite-type oxide is adiabatic small polaron hopping mechanism, which can be expressed by [25]

$$\sigma = \left(\frac{A}{kT} \right) \exp \left(\frac{-E_a}{kT} \right) \qquad (6)$$

where A is material constant containing the carrier concentration term, E_a is the activation energy for hopping conduction, k is Boltzmann constant and T is the absolute temperature. Fig. 6 is the Arrhenius plots of conductivities of SSCC. As can be seen, except SSCC37-10 and SSCC37-9505, the Arrhenius plots of conductivity are nearly linear in low temperature range. The nonlinear behavior

Table 3
Calculated activation energies for the electrical conductivity of SSCC based on the adiabatic small polaron hopping mechanism.

Sample ($Sm_xSr_{1-x}Co_{1-y}Ce_yO_{3-\delta}$)		Temp. range (°C)	E_a (eV)
$x = 0.5$	$y = 0$	100–600	0.0301
	$y = 0.05$	100–600	0.0310
	$y = 0.1$	200–650	0.0832
$x = 0.3$	$y = 0$	–[a]	–
	$y = 0.05$	–	–
	$y = 0.1$	200–750	0.0822

[a] The electrical conductivity may follow a nonadiabatic hopping process which presents as a nonlinear variation in the whole temperature range in the Arrhenius plots.

of SSCC37-10 and SSCC37-9505 may due to the nonadiabatic hopping process [25]. The activation energies E_a calculated from the linear part are listed in Table 3. Larger activation energy would be served to impede hopping of electron carrier and decrease the electrical conductivity. Therefore, for samples with $x = 0.5$, the electrical conductivities have a drop when the E_a increased.

3.5. Electrochemical impedance analysis

The cathode performance for SSCC was investigated by the AC impedance spectroscopy based on a symmetrical cell with a two-electrode configuration. ASR is a significant index used to evaluate the performance of cathode, which was determined form the Nyquist plots of the electrochemical impedance spectra. Figs. 7 and 8 show the typical impedance spectra plots tested from 700 to 750 °C in air and the temperature dependence of the ASR of undoped SSC and Ce-doped SSCC cathodes, respectively. It's obvious that the samples with $x = 0.3$ exhibited much lower polarization resistance than that with $x = 0.5$. Compared with undoped SSC cathode, SSCC55-10 and SSCC37-10 cathodes showed both a lower electrode resistance and activation energy. It suggests that SSCC cathodes with Ce doped into B-site, whatever formed single- or two-phase(s), are more beneficial than undoped SSC for oxygen electrochemical reduction. In addition, it's generally accepted that an ideal SOFC cathode should possess high electronic conductivity (100 S cm^{-1}) at the desired operating temperatures [26]. Low electrical conductivity would increase the charge-transfer resistance for oxygen reduction reaction (ORR) [27–29]. Zhou et al. studied the kinetics of ORR on the $SrSc_{0.2}Co_{0.8}O_{3-\delta}$ cathode by ac impedance, which revealed that the charge-transfer process was the rate-determining step due to the extremely low electrical conductivity of $SrSc_{0.2}Co_{0.8}O_{3-\delta}$ [29]. Fortunately, under the fuel cell operating conditions (400–750 °C), the electrical conductivity of Ce-doped SSC is higher than 200 S cm^{-1}, which is sufficiently high for ORR.

Normally, the polarization of cathode is determining by O_2 adsorption/desorption on the surface of electrode, ionic conduction in the bulk electrode and the diffusion of oxygen in the gas phase. For porous SSC cathode the rate-determining step (RDS) of cathodic reaction is dominantly the adsorption/desorption on the surface of electrode, ionic conduction in the bulk electrode [30]. Deseure et al. [31] and Adler et al. [32] concluded that the smaller grain size with high specific surface area would enhance the performance of porous cathode. Decreasing the grain size would increase both the specific electrochemical surface area and the adsorption/desorption surface and then result in decrease of polarization resistance. The SSCC cathode was deposited onto the surfaces of SDC using the spray coating method and then calcined at 1000 °C for 2 h. As can be seen from Fig. 9, a relatively smaller grain size of SSCC55-9505 and SSCC37-9505 was obtained and therefore lead to a lower ASR than undoped SSC.
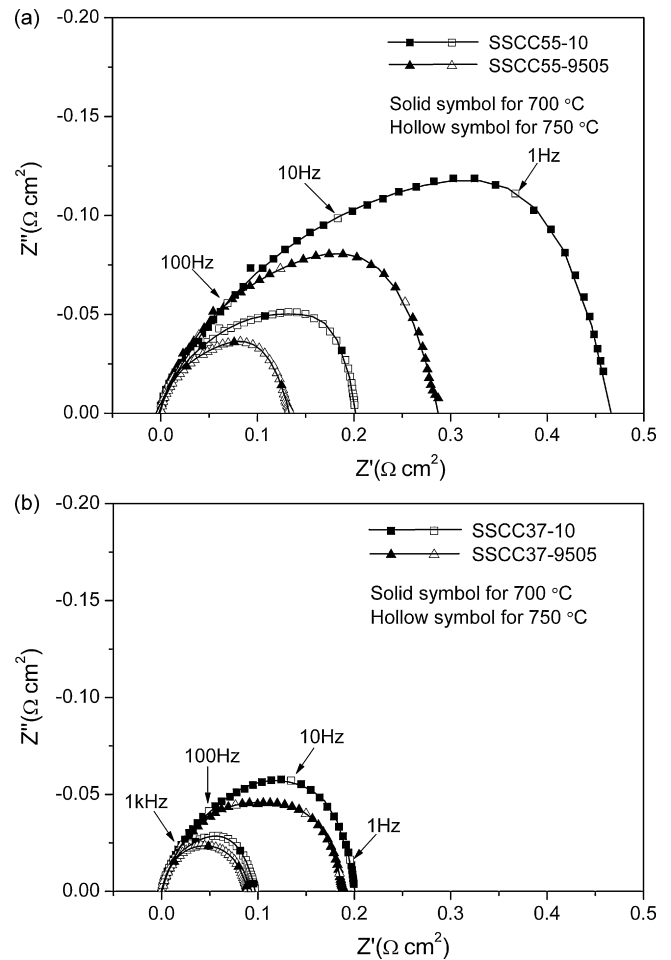

Fig. 7. Impedance spectroscopy for SSCC cathodes in air at 700 and 750 °C: (a) $x = 0.5$; (b) $x = 0.3$.

Perovskite-type mixed conductors, which have a high bulk oxygen vacancy concentration, could conduct oxygen ions through the bulk phase. Sample SSCC55-9505 with larger δ and higher oxygen vacancy concentration than SSCC55-10 could enhance the ionic conduction in the bulk cathode and presented as much lower ASR. Furthermore, the increased oxygen vacancy supplied more active sites for ORR and consequently a reduction of polarization resistance in oxygen adsorption/desorption process [27]. In the case of SSCC37-9505 which has a relatively lower bulk vacancy concen-
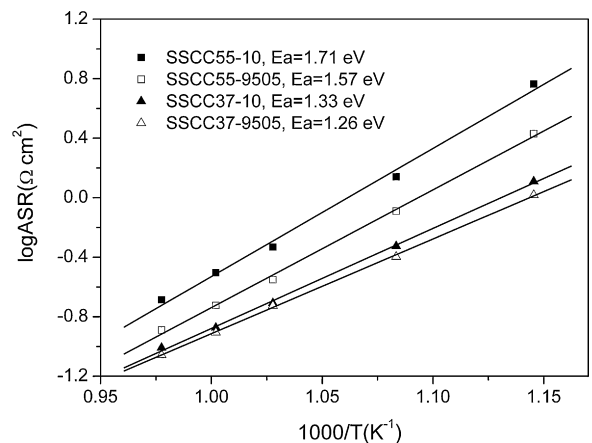

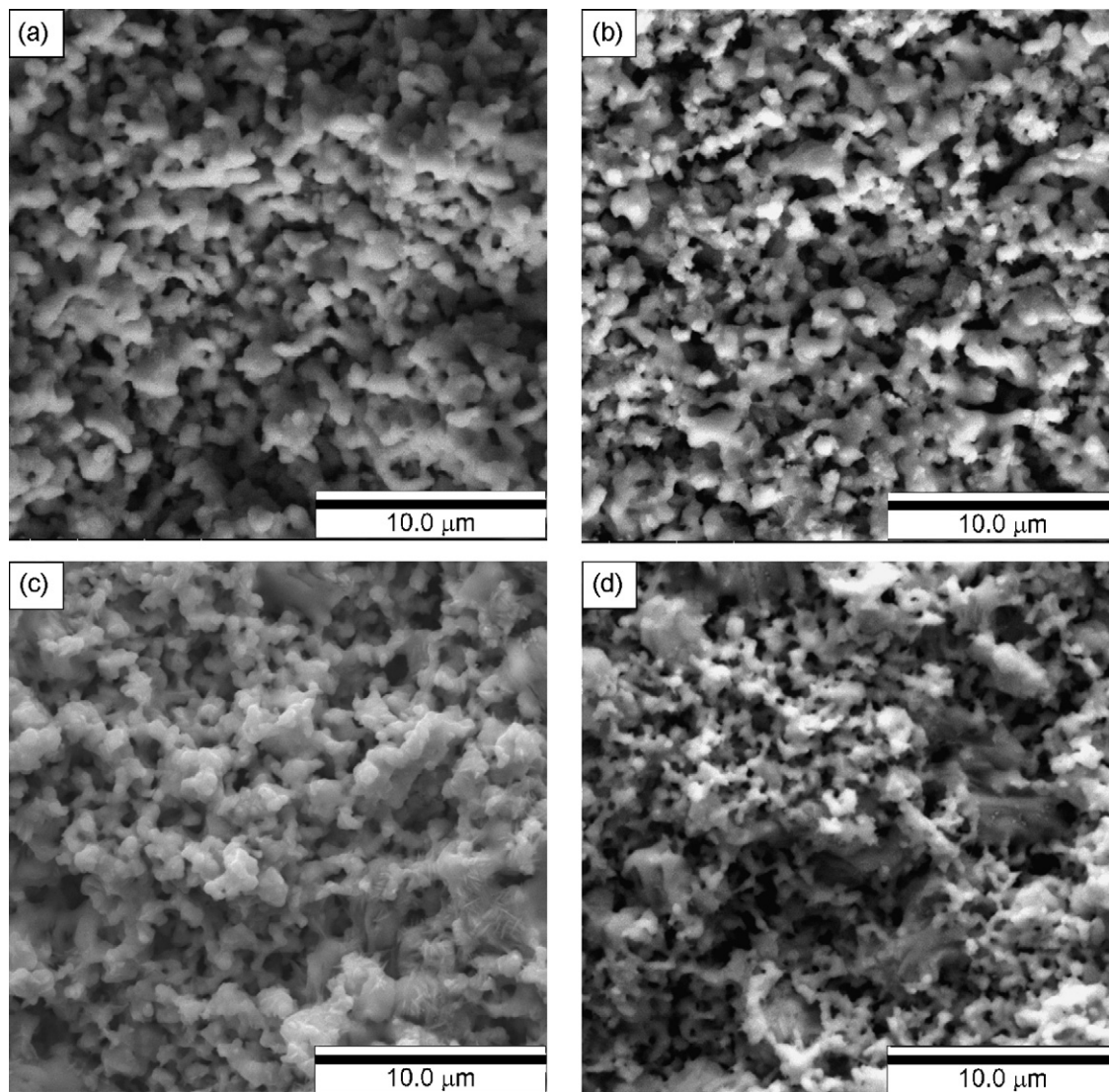**Fig. 8.** Arrhenius plots of the area specific resistance (ASR) for SSCC cathodes.

Fig. 9. SEM images of porous cathode surfaces of SSCC: (a) SSCC55-10; (b) SSCC55-9505; (c) SSCC37-10; (d) SSCC37-9505.

tration, the bulk ionic conduction would be lower than SSCC37-10. However, overall considering the relatively smaller particle size and thereby higher adsorption/desorption surface, SSCC37-9505 still has a decrease in ASR as compared with SSCC37-10.

4. Conclusions

The perovskite-type oxides of cobalt-site cerium doped $Sm_xSr_{1-x}CoO_{3-\delta}$ as potential cathode materials for SOFC have been systematically studied. A phase-pure perovskite-type $Sm_{0.3}Sr_{0.7}Co_{0.95}Ce_{0.05}O_{3-\delta}$ oxide was obtained, while the other samples are actually composed of B-site cation deficient $Sm_xSr_{1-x}Co_{1-y}Ce_{y-z}O_{3-\delta}$ $(0 < z < y)$ and CeO_2 mixed phases. The grain size and electrical conductivity decreased as the Ce content decreased. Moreover, the mechanism of temperature dependence of electrical conductivity is adiabatic hopping of small polaron while samples $Sm_{0.3}Sr_{0.7}CoO_{3-\delta}$ and $Sm_{0.3}Sr_{0.7}Co_{0.95}Ce_{0.05}O_{3-\delta}$ might follow a nonadiabatic hopping mechanism. The oxygen nonstoichiometry δ and TEC of two-phase samples increased with the increase of Ce content while contrary results were obtained for single-phase sample $Sm_{0.3}Sr_{0.7}Co_{0.95}Ce_{0.05}O_{3-\delta}$. Compared with undoped SSC, the lower ASR and activation energy of Ce-doped SSC were observed, where $Sm_{0.3}Sr_{0.7}Co_{0.95}Ce_{0.05}O_{3-\delta}$ exhibited the lowest ASR and activation energy. In addition, the electrode polarization resistance decreased as the Sr doping concentration increased. These results indicated that partial substitution of Co with Ce and the formation of B-site deficiency are effective ways to improve the thermal and electrochemical properties as well as the cathode morphology. In conclusion, B-site Ce-doped $Sm_xSr_{1-x}CoO_{3-\delta}$ oxides were promising candidates as cathode materials in SOFC.

References

[1] S.C. Singhal, Solid State Ionics 135 (2000) 305–313.
[2] B.C.H. Steele, Solid State Ionics 134 (2000) 3–20.
[3] C. Xia, W. Rauch, F. Chen, M. Liu, Solid State Ionics 149 (2002) 11–19.
[4] J.M. Ralph, A.C. Schoeler, M. Krumpelt, J. Mater. Sci. 36 (5) (2001) 1161–1172.
[5] K.T. Lee, A. Manthiram, J. Electrochem. Soc. 153 (2006) 794–798.
[6] H.Y. Tu, Y. Takeda, N. Imanishi, O. Yamamoto, Solid State Ionics 100 (1997) 283–288.

[7] G.Ch. Kostogloudis, N. Vasilakos, Ch. Ftikos, Solid State Ionics 106 (1998) 207–218.
[8] F.W. Poulsen, Solid State Ionics 129 (2000) 145–162.
[9] V. Dusastre, J.A. Kilner, Solid State Ionics 126 (1999) 163–174.
[10] Z.P. Shao, S.M. Haile, Nature 431 (2004) 170–173.
[11] K. Kakinuma, T. Arisaka, H. Yamamura, J. Ceram. Soc. Jpn. 112 (2004) 342–346.
[12] H. Lv, B.Y. Zhao, Y.J. Wu, G. Sun, G. Chen, K.A. Hu, Mater. Res. Bull. 42 (2007) 1999–2012.
[13] X.G. Zhang, M. Robertson, S. Yick, C. Deces-Petit, E. Styles, W. Qu, Y.S. Xie, R. Hui, J. Roller, O. Kesler, R. Maric, D. Ghosh, J. Power Sources 160 (2006) 1211–1216.
[14] C. Suryanarayana, M.G. Norton, X-ray Diffraction: A Practical Approach, Plenum Press, New York, 1998, pp. 223–235.
[15] M.S. Islam, J. Mater. Chem. 10 (2000) 1027–1038.
[16] J.P. Attfield, Int. J. Inorg. Mater. 3 (2000) 1147–1152.
[17] L. Ge, R. Ran, K. Zhang, S.M. Liu, Z.P. Shao, J. Membr. Sci. 318 (2008) 182–190.
[18] E. Konysheva, J.T.S. Irvine, A. Besmehn, Solid State Ionics 180 (2009) 778–783.
[19] X. Dong, Z. Xu, X. Chang, C. Zhang, W. Jin, J. Am. Ceram. Soc. 90 (2007) 3923–3929.
[20] V.V. Kharton, A.A. Yaremchenko, M.V. Patrakeev, E.N. Naumovich, F.M.B. Marques, J. Eur. Ceram. Soc. 23 (2003) 1417–1426.
[21] X.Y. Chen, J.S. Yu, S.B. Adler, Chem. Mater. 17 (2005) 4537–4546.
[22] R.L. Cook, A.F. Sammells, Solid State Ionics 45 (1991) 311–321.
[23] D.R. Askeland, P.P. Phule, The Science and Engineering of Materials, 4th ed., Thomson Brooks/Cole, California, 2003, pp. 53–54.
[24] V. Vashook, D. Franke, J. Zosel, K. Ahlborn, L. Vasylechko, W. Fichtner, U. Guth, Solid State Ionics 179 (2008) 135–142.
[25] L.W. Tai, M.M. Nasrallah, H.U. Anderson, D.M. Sparlin, S.R. Sehlin, Solid State Ionics 76 (1995) 259–271.
[26] W. Zhou, Z.P. Shao, R. Ran, W.Q. Jin, N.P. Xu, Chem. Commun. 44 (2008) 5791–5793.
[27] W. Zhou, R. Ran, Z.P. Shao, W. Zhuang, J. Jia, H.X. Gu, W.Q. Jin, N.P. Xu, Acta Mater. 56 (2008) 2687–2698.
[28] W. Zhou, R. Ran, Z.P. Shao, W.Q. Jin, N.P. Xu, J. Power Sources 182 (2008) 24–31.
[29] W. Zhou, B.M. An, R. Ran, Z.P. Shao, J. Electrochem. Soc. 156 (2009) B884–B890.
[30] M. Koyama, C.J. Wen, T. Masuyama, J. Otomo, H. Fukunaga, K. Yamada, K. Eguchi, H. Takahashi, J. Electrochem. Soc. 148 (2001) A795–A801.
[31] J. Deseure, Y. Bultel, L. Dessemond, E. Siebert, Electrochim. Acta 50 (2005) 2037–2046.
[32] S.B. Adler, Solid State Ionics 111 (1998) 125–134.